RSC Advances

PAPER

Check for updates

AgBr/g-C₃N₄ nanocomposites for enhanced visible-light-driven photocatalytic inactivation of *Escherichia coli*†

Sihui Zhan,[a] Qianlei Hou,[a] Yi Li, [b] Shuanglong Ma,[a] Pengfei Wang,[a] Yanan Li[a] and Haitao Wang [*a]

Visible-light-driven photocatalytic disinfection is highly desired for water treatment due to its advantages such as wide applicability and being free of disinfection byproducts. In this study, AgBr/g-C₃N₄ hybrid nanocomposites were evaluated as photocatalysts under visible light irradiation for water disinfection using *Escherichia coli* as a model pathogen. The physicochemical and photo-electrochemical properties of the photocatalyst were systematically characterized using advanced techniques including scanning electron microscopy (SEM), transmission electron microscopy (HRTEM), powder X-ray diffraction (XRD), UV-visible diffuse reflectance spectra (DRS), X-ray photoelectron spectroscopy (XPS), photoluminescence (PL) spectra and electron spin resonance (ESR) spectroscopy. The inactivation mechanism of *E. coli* was systematically investigated by monitoring the morphology change of the bacteria and analyzing the role of reactive species. The optimized AgBr/g-C₃N₄ hybrid photocatalyst exhibited remarkably enhanced visible-light-driven photocatalytic disinfection performance towards *E. coli* over that of pure g-C₃N₄ and AgBr under visible light, which could completely inactivate 10^7 cfu mL^{-1} *E. coli* in 90 min. Quenching studies indicated that h^+ is the main reactive species responsible for inactivating *E. coli*. The mechanism study revealed a Z-scheme charge transfer mechanism between AgBr and g-C₃N₄. The g-C₃N₄ could effectively trap the photogenerated conduction band electrons of AgBr *via* a Z-scheme type of route, thus significantly promoting the electron–hole separation. The trapping of electrons by g-C₃N₄ could facilitate h^+ accumulation, which accounts for the better disinfection performance of AgBr/g-C₃N₄ compared to AgBr and g-C₃N₄.

1. Introduction

According to a recent report by WHO and UNICEF,[1] over 30% of the world population lack access to safe drinking water. Most of these people are from developing countries where water and wastewater infrastructures are often non-existent. In developing countries, people are often forced to rely on contaminated water for potable use. Every year, millions of people die because of severe waterborne diseases.

The traditional water disinfection treatment techniques including UV irradiation, chlorination, and ozonation are very effective against most waterborne pathogens. However, it may be too costly to implement these traditional disinfection treatment techniques in developing regions. Developing point-of-use drinking water treatment methods is applicable to

address this challenge where centralized drinking water treatment facilities are not available.[2,3] Among various techniques proposed, photocatalytic disinfection is one of the most promising methods for point-of-use water treatment. With the irradiation of an appropriate light source, photocatalysts are capable of inactivating waterborne pathogens through the *in situ* formation of highly reactive oxygen species. Since the first photocatalytic bacterial inactivation was reported by Matsunaga *et al.*,[4] numerous efficient photocatalysts have been developed and tested for the photocatalytic inactivation of pathogenic microorganisms.[5,6]

Since around 43% of energy emitted from the sun is in the form of visible light, it is desirable to develop photocatalysts that could efficiently utilize visible light ($\lambda > 420$ nm) to achieve efficient solar energy-driven disinfection.[7,8] Unfortunately, most of the semiconductor photocatalysts, such as TiO_2 and ZnO, can only utilize the UV portion of solar energy, which accounts for less than 4% of the total solar energy.[9] While tremendous progress has been made, it is still a great challenge to develop highly efficient visible-light-active photocatalysts for practical application.[10–13]

a Key Laboratory of Pollution Processes and Environmental Criteria (Ministry of Education), College of Environmental Science and Engineering, Nankai University, Tianjin 300071, P. R. China. E-mail: envwang@nankai.edu.cn; envwang@gmail.com

b Department of Chemistry, Tianjin University, Tianjin 300072, P. R. China

Recently, graphitic carbon nitride (g-C_3N_4), a polymeric metal-free semiconductor made of earth-abundant elements, has attracted great attention because of its appropriate band gap (2.7 eV) and good photochemical and chemical stability.[14–16] Nevertheless, due to small surface area, poor water dispersibility, rapid recombination of photogenerated charge carriers and insufficient visible-light absorption (<470 nm), the photocatalytic activity of g-C_3N_4 needs further improvement.[15] Several strategies, such as element doping,[17,18] and forming heterojunctions by coupling with metal and/or other semiconductors,[19–23] have been proposed to prepare g-C_3N_4 based photocatalysts with improved performance. Coupling g-C_3N_4 with silver-containing compounds, such as Ag_3PO_4,[24] $AgVO_4$,[25] AgW_2O_4,[26] and Ag nanoparticles,[27,28] has been reported to be an effective strategy for enhancing the visible light photocatalytic activity of g-C_3N_4. Silver bromide (AgBr), as an important photosensitive semiconductor with band gap ∼2.6 eV, has been widely used as a photosensitive material in photographic films.[29] The application of pure AgBr is plagued by its poor photostability: it will undergo decomposition to release Ag^+ and Br^- under light irradiation.[30] Therefore, rather than as a photocatalyst, AgBr has been more widely used as a modifier to prepare hybrid photocatalysts since it can facilitate electron–hole separation.[31–36] Previous studies have shown that combining AgBr and g-C_3N_4 into heterojunctions could suppress not only the recombination of charge carriers but also the photocorrosion of AgBr, leading to enhanced photocatalytic performance.[37,38] However, the photocatalytic disinfection properties of the AgBr/g-C_3N_4 heterojunction have not been well studied.

In this study, highly efficient AgBr/g-C_3N_4 nanocomposites were prepared by growth of AgBr nanoparticles on protonated g-C_3N_4. Photocatalytic disinfection activity of the nanocomposites under visible light irradiation is investigated using *E. coli* as a model pathogenic bacterium. The nanocomposites exhibit significantly enhanced photocatalytic bacterial inactivation compared to g-C_3N_4 and AgBr. The effects of AgBr content, solution pH and organic matter on the photocatalytic bacterial inactivation efficiency have been systematically studied. Detailed investigations of reactive species using chemical scavengers and the electron spin resonance (ESR) technique are carried out to determine the bacterial inactivation mechanisms.

2. Experimental

2.1 Materials

All reagents were of analytical grade and used without further purification. Anhydrous ethanol (C_2H_5OH), melamine ($C_3H_6N_6$) and silver nitrate ($AgNO_3$) were obtained from Jiangtian Chemical Technology Co. Ltd (Tianjin, China). Hexadecyltrimethylammonium bromide (CTAB) was purchased from Aladdin Industrial Corporation (Shanghai, China).

2.2 Preparation and protonation of g-C_3N_4

g-C_3N_4 was prepared by a thermal condensation method using melamine as precursor.[26] In a typical process, 10 g melamine powder was placed in a crucible and then covered with a lid. The crucible was placed in a muffle furnace and heated to 550 °C with a heating rate of 5 °C min^{-1} and maintained at this temperature for 4 hours. After cooling down to room temperature naturally, the product was collected and ground into fine powder.

The protonation of g-C_3N_4 was achieved by hydrothermal treatment.[37] Briefly, 500 mg g-C_3N_4 powder was dispersed in 40 mL of 0.2 M H_2SO_4 solution with vigorous stirring. The mixture was transferred to a Teflon-lined stainless steel autoclave with 50 mL capacity and heated at 150 °C for 24 h. After cooling down naturally to room temperature, the product was collected and washed thoroughly with deionized water and ethanol. Finally, the product was dried in air at 80 °C overnight for further use.

2.3 Preparation of the AgBr/g-C_3N_4 nanocomposite

In a typical procedure, 150 mg of protonated g-C_3N_4 was dispersed in 20 mL ethanol with the help of sonication. Then, 50 mL aqueous solution of CTAB was added into the suspension under vigorous stirring and the solution was kept stirring for 12 h. Subsequently, $AgNO_3$ solution was added dropwise and the mixed solution was kept stirring for another 6 h. Finally, the sample was collected by centrifugation, washed thoroughly with deionized water and dried at 80 °C. The hybrid photocatalyst was labelled as AgBr/g-C_3N_4. The weight percentage of AgBr in the hybrid photocatalyst was 30% unless otherwise stated. Pure AgBr was prepared using an identical method without the presence of g-C_3N_4.

2.4 Characterization

The phase and morphology of the samples were characterized using X-ray diffraction (XRD, Rigaku D/Max 2500PC), transmission electron microscopy (TEM, JEOL model JEM-1200EX) and scanning electron microscopy (SEM, Hitachi SU8010, Japan). The functional groups on the surface of the samples were characterized using a Nicolet 5DX-FTIR spectrometer with KBr as a reference. X-ray photoelectron spectroscopy (XPS) data were collected with a Thermo ESCALAB250 spectrometer to get bonding information of Ag, Br and C elements. Nitrogen adsorption–desorption isotherms were obtained with a Quantachrome Autosorb automated gas sorption system (Quantachrome Instruments, USA), and the isotherms were analyzed using the Barrett–Joyner–Halenda (BJH) model. Photoluminescence (PL) and photoresponse techniques were employed to evaluate the photoelectrochemical properties of the photocatalysts. ESR spectra were obtained with a Magnet TechMS400 spectrometer.

2.5 Photocatalytic inactivation of *E. coli*

All materials used in the experiments were carefully sterilized. The photocatalytic inactivation of *E. coli* was carried out in a cylindrical glass reactor with double-walled cooling-water jacket. The *E. coli* cells were cultured at 37 °C in a shaking incubator. After a satisfactory cell density was obtained, the *E. coli* cells were harvested by centrifugation and washed

thoroughly with sterilized 0.85% (w/v) saline solution. The final density of *E. coli* was diluted to *ca.* 10^7 cfu mL^{-1} using 0.85% (w/v) saline solution for disinfection experiments.

For all disinfection experiments, photocatalysts were dispersed in saline solution to get a 4 mg mL^{-1} suspension. Typically, 250 μL of photocatalyst suspension was added to 10 mL of *E. coli* solution under constant stirring. The disinfection experiments were initiated by irradiating the solution using a 300 W xenon lamp with a UV cutoff ($\lambda < 420$ nm). The solution was sampled at planned times and the density of *E. coli* was determined using the standard plate count method. All bacterial disinfection experiments were repeated three times.

The morphology change of *E. coli* during the inactivation process was investigated with SEM. The death tendency of *E. coli* was studied using the fluorescence-based cell live/dead test.

3. Results and discussion

3.1 Characterization of AgBr/g-C$_3$N$_4$ nanocomposites

The crystal structure of g-C$_3$N$_4$ and AgBr/g-C$_3$N$_4$ hybrid photocatalysts were analyzed by XRD. As shown in Fig. 1a, all of the peaks in the XRD patterns of the samples could be easily indexed to the hexagonal g-C$_3$N$_4$ (JCPDS 87-1526) and cubic AgBr (JCPDS 6-438). No impurity peaks are observed in the XRD patterns except that of g-C$_3$N$_4$ and AgBr, suggesting that the as-synthesized samples are of pure phases. The XRD pattern of g-C$_3$N$_4$ exhibits two characteristic diffraction peaks at 27.7 and 13.1° that can be well ascribed to (002) and (100) diffraction planes, respectively. These two characteristic peaks are consistent with the previous results of g-C$_3$N$_4$. The prominent peak at 27.7° is ascribed to the interplanar stacking of aromatic units. The peak at 13.3°, with a much weaker intensity, corresponding to a distance $d = 0.681$ nm, is associated with interlayer stacking motif of tri-*s*-triazine units.[39] The XRD pattern of pristine g-C$_3$N$_4$ is also shown as a comparison, which exhibits the same diffraction peaks as protonated g-C$_3$N$_4$. The results indicate that the typical layered structure of g-C$_3$N$_4$ is well kept and the protonation treatment does not change the phase of g-C$_3$N$_4$. For the XRD pattern of AgBr, the peaks at 26.8°, 30.9°, 44.4°, 55.1°, 64.5° and 73.3° are the corresponding plane reflections of (111), (200), (220), (222), (400) and (420) of the cubic AgBr, indicating that the sample is pure well-crystallized AgBr crystals. For AgBr/g-C$_3$N$_4$ nanocomposites, the diffraction pattern shows the coexistence of the diffraction peaks of both g-C$_3$N$_4$ and AgBr.
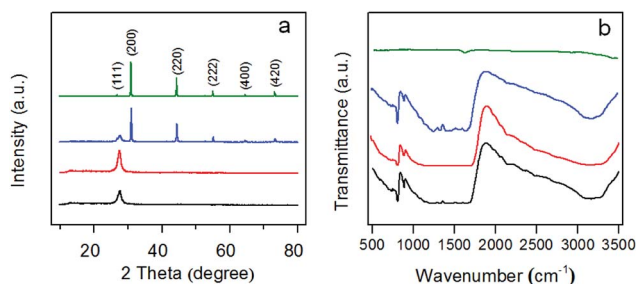
With an increase of AgBr content, the relative intensity of the characteristic peaks of AgBr in the XRD pattern keeps increasing while that of the g-C$_3$N$_4$ keeps decreasing (Fig. S1a†). The narrow sharp peaks suggest that the AgBr in the hybrid photocatalysts is of high crystallinity.

FT-IR was used to identify the functional groups of as-prepared photocatalysts. Protonated g-C$_3$N$_4$ exhibits a similar FT-IR spectrum to that of pristine g-C$_3$N$_4$ (Fig. 1b), which is in accordance with a previous report by Ong *et al.*[40] The wide peak at about 3200 cm^{-1} could be assigned to the stretching vibrations of N–H and O–H. The strong absorption peaks in the region of 1200–1650 cm^{-1}, centered at 1635, 1572, 1416, 1325 and 1249 cm^{-1}, are due to the characteristic stretching vibrations of C–N and C=N heterocycles.[41] Additionally, the sharp peak at around 812 cm^{-1} is attributed to the characteristic breathing mode of tri-*s*-triazine units.[42] Compared with g-C$_3$N$_4$, AgBr shows weak IR absorption. All of the AgBr/g-C$_3$N$_4$ hybrid photocatalysts therefore show analogous spectra due to the strong IR response of g-C$_3$N$_4$ (Fig. S1b†).

The morphology and microstructure of g-C$_3$N$_4$ and AgBr/g-C$_3$N$_4$ samples were characterized using TEM and SEM. As shown in Fig. 2a and c, g-C$_3$N$_4$ exhibits a porous network structure caused by the protonation treatment. During the hydrothermal process, g-C$_3$N$_4$ may decompose to form pores and defects on g-C$_3$N$_4$. As a comparison, pristine g-C$_3$N$_4$ exhibits a 2D lamellar structure composed of multiple nanosheets without apparent pores (Fig. S2a and S2b†), which was in accordance with reported results.[43,44] The lateral size of protonated g-C$_3$N$_4$ is apparently smaller than that of pristine g-C$_3$N$_4$, indicating the decomposition of condensed triazine rings to clusters/oligomers. The porous structure leads to a larger
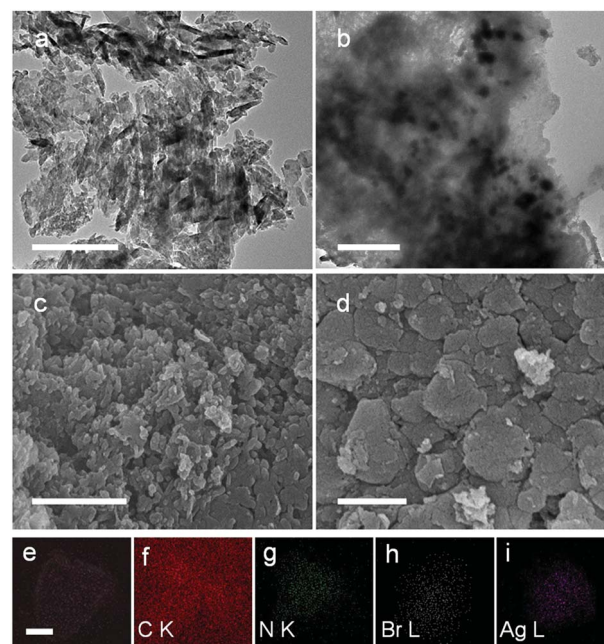

Fig. 1 (a) XRD patterns and (b) FT-IR spectra of pristine g-C$_3$N$_4$ (black), protonated g-C$_3$N$_4$ (red), AgBr/g-C$_3$N$_4$ (blue) and AgBr (olive).

Fig. 2 TEM and SEM images of protonated g-C$_3$N$_4$ (a and c) and AgBr/g-C$_3$N$_4$ (b and d). SEM image of AgBr/g-C$_3$N$_4$ (e), and corresponding element mapping for C (f), N (g), Br (h) and Ag (i) elements. The scale bars are 500 nm.

specific surface area and provides abundant active sites for the growth of AgBr nanoparticles. Fig. 2b clearly shows the growth of AgBr nanoparticles with size around 100 nm uniformly dispersed on g-C_3N_4. The protonation treatment played an important role in the synthesis of AgBr/g-C_3N_4 hybrid photocatalyst; only very few AgBr nanoparticles can sporadically grow on the g-C_3N_4 nanosheets without treatment (result not shown). The AgBr particles synthesized in the absence of g-C_3N_4 exhibit apparently larger size up to 3 microns (Fig. S2c†). According to the classical nucleation and growth theory, homogeneous nucleation occurs with much more difficulty than heterogeneous one.[45] Without the presence of g-C_3N_4, the nuclei formed at the initial stage are very limited and will result in the growth of larger particles. This result suggests that the abundant pores and defects on g-C_3N_4 could serve as the heterogeneous nucleation sites for growth AgBr nanoparticles. Compared with g-C_3N_4, the surface of the hybrid photocatalyst is much smoother, which can be attributed to the filling of pores of protonated g-C_3N_4 by AgBr nanoparticles. Fig. 2e is a representative SEM image of AgBr/g-C_3N_4 hybrid photocatalyst and Fig. 2f–i are the corresponding EDS elemental mappings for C, N, Br and Ag elements. On the elemental maps, the intensity of the brightness is correlated to the concentration of the corresponding element. The distribution of Br and Ag elements suggests that AgBr nanoparticles are well dispersed on g-C_3N_4.

The nitrogen adsorption–desorption isotherms and BJH pore size distribution plots of as-prepared samples are presented in Fig. 3. Except g-C_3N_4, the other two samples exhibit a type IV isotherm with H3 hysteresis loop (Fig. 3a), indicating the existence of pores in protonated g-C_3N_4 and AgBr/g-C_3N_4 samples. The specific surface areas of g-C_3N_4, protonated g-C_3N_4 and AgBr/g-C_3N_4 are 12.23, 55.94, 37.93 m^2 g^{-1}, respectively. The corresponding curves of pore size distributions (Fig. 3b) confirm that all samples have a broad pore size distribution ranging from 5 to 30 nm with maximum at 8 nm. The results clearly show that protonation treatment significantly expands the percentage of pores with smaller size, corroborating the TEM and SEM results. The percentage of small pores decreased after growth of AgBr nanoparticles, indicating the blockage of small pores by AgBr nanoparticles. The results clearly show that protonation treatment could significantly increase the specific surface area as well as the pore volume of g-C_3N_4. Assuming the shape of AgBr nanoparticles is close to spherical, based on the average size and

density of AgBr, the theoretical specific area of AgBr can be estimated as 9 m^2 g^{-1}. Combining AgBr with g-C_3N_4 therefore produces hybrid photocatalysts with specific surface area smaller than that of g-C_3N_4. Moreover, since defects are the most reactive sites on protonated g-C_3N_4 matrix, the AgBr nanoparticles would be preferentially formed on the defects to form a homogeneous nanocomposite photocatalyst. The formation of AgBr nanoparticles on the g-C_3N_4 matrix would cause some blocking of the pores of g-C_3N_4, which will also contribute to the decrease of the specific surface area.

The XPS technique was employed to further investigate the chemical composition and identify the chemical status of the elements in the samples (Fig. 4 and S3†). The XPS survey scan spectrum confirms that g-C_3N_4 is made up of C, N and O elements (Fig. S3†). The presence of oxygen originates from the adsorption of oxygen from the atmosphere in the sample preparation process.[46] For the hybrid photocatalyst, besides C, N and O elements, the existence of Ag and Br is observed. The C 1s spectrum in Fig. 4a shows two peaks centered at 284.8 and 288.4 eV. The peak at 284.8 eV is typically assigned to graphitic carbon atoms from adventitious carbon.[47] The peak at 288.4 eV, corresponding to N=C–N_2 is attributed to sp^2-hybridized carbon with three N neighbors.[48,49] Fig. 4b presents the XPS spectrum of N 1s, which could be deconvoluted into three peaks with binding energies of 398.8, 400.3 and 404.7 eV. The main component at 398.8 eV could be attributed to sp^2-hybridized N in triazine rings (C=N–C).[50] The peak at 400.3 eV is ascribed to the bridging nitrogen atoms in the aromatic cycles (N–(C)$_3$).[51] The third peak at 404.7 eV is associated with positive charge localization in heterocycle owing to the protonation of g-C_3N_4.[22,52] The two peaks in the Ag spectrum could be ascribed to Ag 3d$_{5/2}$ at 368.0 eV and Ag 3d$_{3/2}$ at 374.0 eV (Fig. 4c).[53] The Br spectrum comprises two individual peaks, Br 3d$_{5/2}$ and Br 3d$_{3/2}$, with binding energies of 68.0 eV and 69.0 eV, respectively (Fig. 4d).[54] The atomic ratio of Ag to Br is 1.18, suggesting the nanocomposite may contain a few Ag nanoclusters.
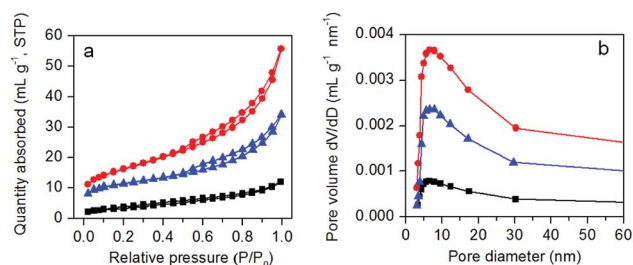
Fig. 3 Nitrogen adsorption–desorption isotherms (a) and pore diameter distributions (b) of pristine g-C_3N_4 (black), protonated g-C_3N_4 (red), and AgBr/g-C_3N_4 (blue).
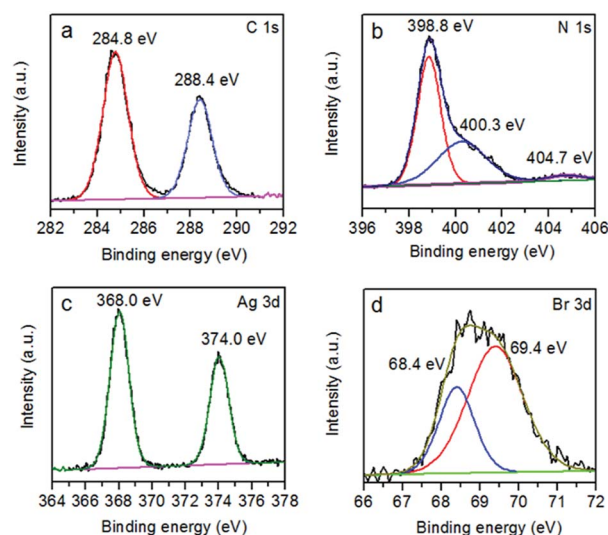
Fig. 4 High resolution XPS spectra of (a) C 1s, (b) N 1s, (c) Ag 3d and (d) Br 3d of AgBr/g-C_3N_4.

3.2 Photocatalytic inactivation of *E. coli*

The visible-light-driven photocatalytic disinfection performance of g-C$_3$N$_4$, AgBr and AgBr/g-C$_3$N$_4$ hybrid photocatalysts were evaluated using *E. coli* as a bacterial model. No apparent decrease of viable cell density is observed for dark control experiment (Fig. 5a), revealing the low cytotoxic nature of our sample towards *E. coli* without visible light irradiation. It is clearly shown in Fig. 5b that the viable cell density keeps constant in the blank control experiment, suggesting that the visible light has no negative effect on the cell viability. Both g-C$_3$N$_4$ and AgBr exhibit poor disinfection efficiency for inactivating *E. coli*. Only 0.61 and 0.36 log decrease in cell density is observed after visible light irradiation for 90 min for g-C$_3$N$_4$ and AgBr, respectively. This number is comparable to that for the dark control. Their weak disinfection activity could be therefore attributed to the rapid recombination of photogenerated charge carriers.[6] On the contrary, AgBr/g-C$_3$N$_4$ nanocomposites exhibit significantly enhanced disinfection activity (Fig. 5b). The hybrid photocatalyst with 30% AgBr shows the best disinfection performance under visible light irradiation, which completely inactivates *E. coli* in 90 min. The results indicate that coupling of AgBr with g-C$_3$N$_4$ could effectively suppress the recombination of photogenerated charge pairs, leading to the enhancement of disinfection efficiency.[55] Fig. 5c presents a plot of the inactivation efficiency against the AgBr percentage, the curve exhibiting a V-shape. The optimal loading of AgBr is *ca.* 30%; further increase of the loading amount will cause a decrease in performance due to blockage of the light path to g-C$_3$N$_4$. To investigate the enhancement mechanism, a control experiment was carried out using mechanically mixed g-C$_3$N$_4$ and AgBr as photocatalyst. Comparing with g-C$_3$N$_4$ and AgBr, the photocatalytic disinfection efficiency was greatly improved by simply mixing these two components. This result suggests that charge transfer could easily happen between g-C$_3$N$_4$ and AgBr. However, the enhancement is much weaker when compared with AgBr/g-C$_3$N$_4$. These results confirm the existence of the heterostructures between AgBr and g-C$_3$N$_4$ in the photocatalysts, which contribute to enhancement of the photocatalytic disinfection performance.

3.3 Fluorescence-based cell live/dead test

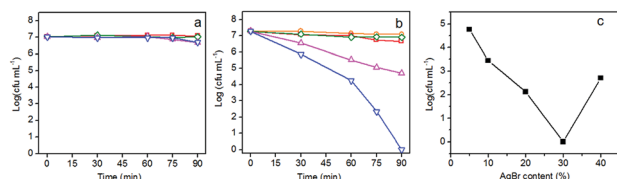To investigate the photocatalytic disinfection process of AgBr/g-C$_3$N$_4$ towards *E. coli*, the cell viability was measured with a live/dead fluorescence assay kit after exposure to light irradiation for

Fig. 5 Inactivation efficiency toward *E. coli* (10^7 cfu mL^{-1}) (a) in the dark and (b) under visible light irradiation with g-C$_3$N$_4$ (red square), AgBr/g-C$_3$N$_4$ (blue down triangle), AgBr (green diamond), physically mixed AgBr and g-C$_3$N$_4$ (magenta up triangle) and light control (orange circle). (c) Plot of the final cell density in the solution after disinfection experiment against AgBr percentage.
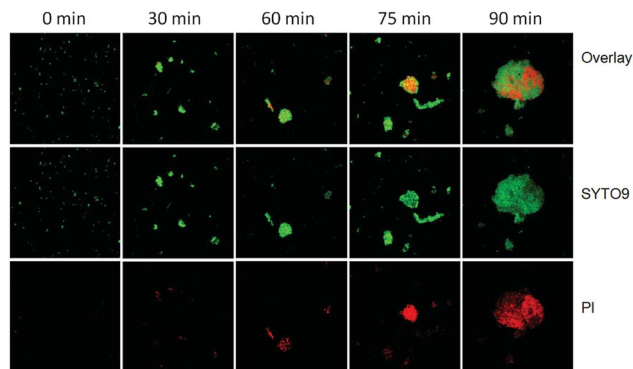

Fig. 6 Confocal fluorescence images of live and dead *E. coli* cells during the photocatalytic disinfection process. Each image size is 185 × 185 μm^2.

different times. The DNAs of *E. coli* cells were stained with a mixed solution of two fluorescent dyes, SYTO9 and PI. SYTO9 is a cell-permeable green fluorescent dye labeling both live and dead cells, whereas PI is a cell-impermeable red fluorescent dye labeling only membrane-compromised cells. Prior to starting the experiment, only very few dead *E. coli* cells resulting from natural cell death are observed (Fig. 6). After 30 min, a small amount cells displaying red fluorescence are observed, implying the integrity of some bacterial cells is lost. Sixty minutes later, most of the *E. coli* cells adsorbed on the photocatalyst are dead (exhibiting red fluorescence), while a considerable number of *E. coli* cells in the free state are still alive. This result clearly shows that adsorption of bacteria onto the photocatalyst is the first step in the inactivation process. With the time extended to 75 min, most of the bacteria are agglomerated together and stained red. At 90 min, nearly all *E. coli* cells are agglomerated together into big clusters and dead. The results suggest that the bacterial cells are most likely killed by the direct attack of reaction species from the surface of the photocatalyst rather than reactive species diffused into the bulk solution.

3.4 Destruction of *E. coli* cells visualized by SEM

The morphology change of *E. coli* cells during the photocatalytic disinfection process was characterized using SEM. Prior to experiment, *E. coli* cells with smooth and intact membrane normally display a rod-shaped structure with average length of *ca.* 1 μm (Fig. 7a). Interestingly, it appears that one *E. coli* cell has just completed cell division. After 30 min, obvious pit deformation of the *E. coli* cell wall happened (Fig. 7b), implying the oxidation and destruction of the outer membrane of *E. coli* by photogenerated reactive species. The length of the *E. coli* cell is about 1.96 μm, almost two times that of a normal one. Cell elongation is a typical SOS response when exposed to detrimental biocides and UV irradiation, suggesting the cell is facing attack by photogenerated reactive species.[56] With the extending of the disinfection time, cells with large cavities as well as severe elongation are observed, indicating the severe damage of the cell envelope. After 75 min, the cells exhibit plate instead of rod shape, indicating the leakage of cytoplasm through damaged
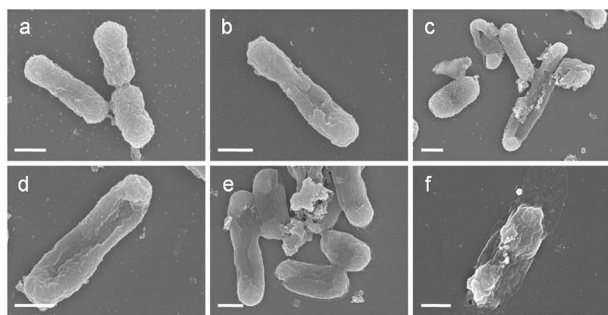
Fig. 7 SEM images of *E. coli* treated with AgBr/g-C$_3$N$_4$ (100 μg mL^{-1}) under visible light irradiation for (a) 0, (b) 30, (c) 45, (d) 60, (e) 75 and (f) 90 min. Scale bar is 500 nm.

Fig. 8 Influence of (a) pH and (b) humic acid on the photocatalytic disinfection performance.

cell membrane. After 90 min, the shape of each *E. coli* cell is severely deformed and parts of the cell are really flat due to the loss of cell inclusions. These results indicate that the destruction of *E. coli* cells firstly starts from the cell membrane and proceeds to the intracellular components with time, leading to the death of *E. coli* cells.

3.5 The effect of Ag$^+$ ions

It is well known that AgBr is not stable under light irradiation and will undergo decomposition to release Ag$^+$ into solution. To elucidate the effect of Ag$^+$ on the disinfection performance of the photocatalysts, the Ag$^+$ concentration during the disinfection experiment was monitored. During the photocatalytic disinfection process, the concentrations of Ag$^+$ in the solution were *ca.* 0.16 and 0.13 ppm for AgBr and AgBr/g-C$_3$N$_4$, respectively, as determined by ICP. According to our previous study,[26] 0.5 ppm Ag$^+$ can only result 0.62 log removal of *E. coli* in 90 min. So, the contribution of Ag$^+$ to the disinfection performance of the photocatalysts was negligible.

3.6 Influence of pH and humic acid

The pH of the solution during the photocatalytic disinfection process is usually considered to be an important factor since pH has a significant influence on the adsorption of bacteria on the photocatalyst. Moreover, the pH of water contaminated by pathogenic bacteria may vary due to the metabolic activity of the bacteria. The influence of pH on the photocatalytic inactivation of *E. coli* was studied by adjusting the pH of the solution while keeping other parameters constant. The solution pH shows negligible influence on the disinfection efficiency (Fig. 8a). The high tolerability of AgBr/g-C$_3$N$_4$ to pH would be beneficial for its practical use. Humic acid (HA) is the most common natural organic matter which widely exists in natural water. Originating from the decomposition of plants and animals, HA is composed of a hydrophobic aromatic core that is highly substituted with functional groups including alcohol, carboxyl, phenolic-OH, hydroxyl, carbonyl, amide, amine, and quinone. As shown in Fig. 8b, HA exhibits significant influence on disinfection efficiency of the nanocomposites in a dose-dependent manner. The disinfection efficiency shows apparent decrease when the concentration of HA is above 0.5 mg L^{-1}. There are carboxyl, amidogen, and hydroxyl groups on the surface of cell
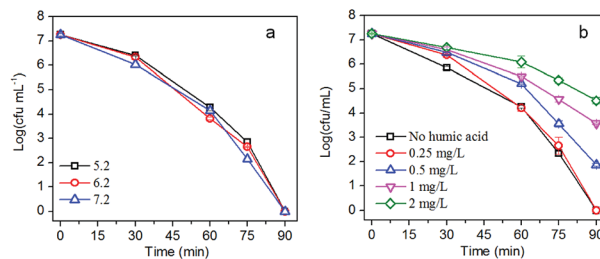
membrane and cell wall of *E. coli*. Moreover, most nucleic acids, proteins, and other biomacromolecules contain aromatic rings. Given the structure of HA, *E. coli* and HA may interact with each other through forming hydrogen and π–π bonds. At higher concentration, HA would retard the collision between *E. coli* cells and photocatalysts. As confirmed by the fluorescence result, adsorption of *E. coli* is the first step for the disinfection process, and blocking the contact of *E. coli* and photocatalyst will definitely result in a decrease of the disinfection efficiency. HA can also absorb a broad spectrum of light; it therefore could mitigate the detrimental impacts of light irradiation on *E. coli*.[57] Moreover, HA will compete with *E. coli* cells for reactive species, which also will lead to a decrease of disinfection efficiency.[26]

3.7 Mechanism of improved photocatalytic disinfection

The photocatalytic disinfection performance of the photocatalyst is closely related to its photo-electrochemical properties. To investigate the enhanced mechanism of photocatalytic disinfection of AgBr/g-C$_3$N$_4$, we first measured the UV-visible diffuse reflectance spectra of the as-prepared samples (Fig. 9a). The calculated band gap energy of pristine g-C$_3$N$_4$ is 2.7 eV, which is lower than that of protonated g-C$_3$N$_4$ (2.78 eV), indicating that protonation treatment can cause a blue shift.[58] This blue-shift phenomenon could be attributed to the weakening of the π-conjugated system due to the formation of pores.[59] Comparing with g-C$_3$N$_4$, introducing AgBr to g-C$_3$N$_4$ matrix can only cause minimal changes in the absorption edge, while the absorption intensity in the visible region is significantly enhanced. Generally, the enhancement of absorption in the visible region increased with an increase of the percentage of AgBr. This enhancement could be ascribed to the formation of heterojunctions between AgBr and g-C$_3$N$_4$. The enhancement of visible light absorption can increase the production rate of free electrons and holes, which is beneficial for photocatalytic disinfection.

To investigate the recombination and lifespan of photogenerated electron–hole pairs in the photocatalysts, the PL emission spectra of the samples were examined. As shown in Fig. 9b, all of the samples exhibit a similar shape with broad emission peak centered at 455 nm. Protonation treatment as well as AgBr doping can significantly weaken the intensity of the PL emission of g-C$_3$N$_4$. It is believed that the intensity of PL is positively correlated to the recombination probability of photogenerated charge carriers. The significant drop of the PL intensity of AgBr/g-C$_3$N$_4$ indicates that AgBr doping can
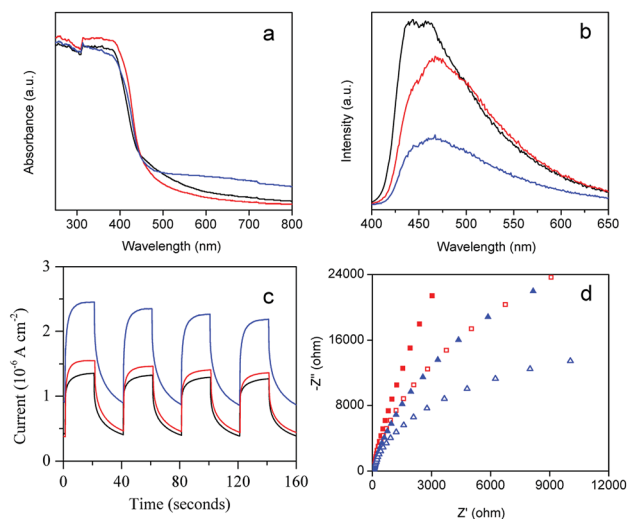
Fig. 9 (a) UV-visible diffuse reflectance and (b) PL spectra of pristine g-C_3N_4 (black), protonated g-C_3N_4 (red) and AgBr/g-C_3N_4 (blue). (c) Photocurrent response curves and (d) Nyquist plots of g-C_3N_4 (red) and AgBr/g-C_3N_4 (blue). Solid symbols represent data obtained in the dark while open ones represent data obtained with visible light irradiation.

effectively prevent the recombination of photogenerated electron–hole pairs. AgBr/g-C_3N_4 exhibits the lowest emission peak intensity (Fig. S4†), illustrating the lowest recombination of photogenerated charge carriers. The results are highly consistent with the photocatalytic disinfection result (Fig. 5b).

The transient photocurrent responses have been demonstrated to be a useful method to investigate the separation of photogenerated electron–hole pairs of the photocatalysts. Fig. 9c displays the results of the photocurrent response of g-C_3N_4 and AgBr/g-C_3N_4 with several on–off cycles of intermittent visible light irradiation. The photocurrent is formed from the separation and diffusion of the photoinduced electrons and holes.[40] The current value dropped rapidly as the incident light was switched off and returned to the original value instantaneously when the light was switched on again. The quick on/off response of the photocurrent to visible light could be attributed to the rapid separation and transfer of the photogenerated charges on the surface of the prepared working electrodes. There is no appreciable difference in the photocurrent response time of the two photocatalysts, whereas the current value of the AgBr/g-C_3N_4 sample is much higher than that of g-C_3N_4, indicating more photogenerated charge carriers. The result suggests the heterojunctions formed between AgBr and g-C_3N_4 could efficiently promote the generation as well as separation of photogenerated electron–hole pairs.[60] The results of photocurrent response together with the PL spectra results indicate that the efficient charge separation is the most important factor for the performance enhancement of AgBr/g-C_3N_4.

Electrochemical impedance spectra of g-C_3N_4 and AgBr/g-C_3N_4 were examined to determine their charge transfer resistance. As shown in the Nyquist plots in Fig. 9d, the arc radius of AgBr/g-C_3N_4 is smaller compared with g-C_3N_4 under visible light, indicating the better charge transfer ability of AgBr/g-C_3N_4

than g-C_3N_4. The arc radius of AgBr/g-C_3N_4 is also smaller than that of g-C_3N_4 in the dark, suggesting that AgBr loading facilitates charge transfer even in dark condition.

3.8 Analysis of reactive species

It is well known that reactive species including O_2^-, H_2O_2, OH, e^-, and h^+ play important roles in photocatalytic disinfection processes.[6,26] The role of different reactive species varies for different photocatalysts. In order to clarify the role of reactive species in our system, different scavengers were introduced into the disinfection system to remove the corresponding reactive species. Ethylenediaminetetra-acetic acid disodium salt (EDTA-2Na), Cr(VI) and isopropanol were used as scavengers for h^+, e^- and ·OH, respectively. As is clear in Fig. 10a, adding EDTA-2Na into the experimental system caused the greatest drop in disinfection efficiency, suggesting that h^+ is the main reactive species in the disinfection process. The addition of isopropanol (OH scavenger) and Cr(VI) (e^- scavenger) can also cause apparent decrease of disinfection efficiency, suggesting that ·OH and e^- are also involved in the disinfection process. Based on these results, h^+ is supposedly the main reactive species in the photocatalytic disinfection process, although ·OH and e^- are also involved. Given h^+ can only exist on the surface of the photocatalyst, direct contact between E. coli and photocatalyst is therefore very important for inactivating E. coli. The results are consistent with the fluorescence assay and humic acid experiment which both suggest the critical role of direct contact in inactivating E. coli cells.

To further investigate radical generation during the photocatalytic disinfection process, the ESR technique with DMPO as trapping agent was employed to detect the production of ·OH and ·O_2^- (Fig. 10b). As shown in Fig. 10b, no distinct signals could be observed for both ·OH and ·O_2^- radicals in the dark. After visible light irradiation for 5 min, quadruple characteristic peaks for the DMPO–·OH adduct with an intensity ratio of 1 : 2 : 2 : 1 could be observed, confirming the formation of ·OH via the OH^-/H_2O oxidation by holes.[61,62] Given that ·O_2^- radicals are very unstable and undergo disproportionation easily rather than slowly reacting with DMPO, DMPO–O_2^- adducts were detected in methanol. According to Fig. 10c, six characteristic peaks of the DMPO–·O_2^- adducts derived from O_2 reduction by electrons are observed.[63,64] It is also clear that the signal of ·O_2^- is much stronger than that of ·OH. The results confirmed that ·OH and ·O_2^- were produced by AgBr/g-C_3N_4
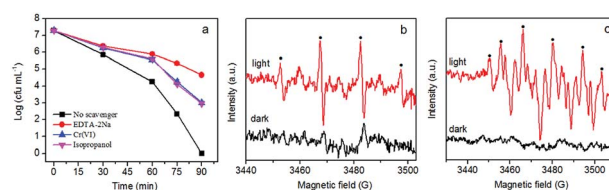
Fig. 10 (a) Photocatalytic disinfection efficiency of AgBr/g-C_3N_4 (100 µg mL^{-1}) towards E. coli (10^7 cfu mL^{-1}) with different scavengers (0.1 mM EDTA-2Na, 0.02 mM Cr(VI), 0.5 mM isopropanol) under visible light. ESR spectra of AgBr/g-C_3N_4 in (b) H_2O and (c) methanol with DMPO as a radical trapper.
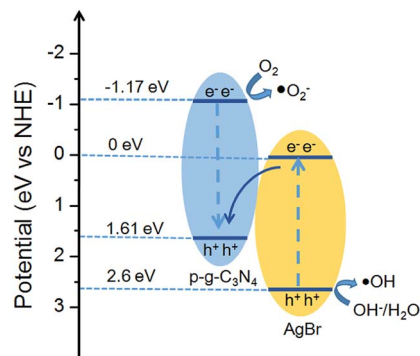
Fig. 11 Z-scheme charge transfer mechanism over AgBr/g-C_3N_4 under visible light irradiation.

nanocomposite under visible light illumination, presenting solid evidence that photogenerated holes and electrons could remain long enough to react with dissolved oxygen/H_2O to form $\cdot OH$ and $\cdot O_2^-$.

3.9 Disinfection mechanism

Based on the data derived from UV-visible DRS, the potentials of conduction band (CB) and valence band (VB) edges of g-C_3N_4 (AgBr) are determined to be −1.17 eV (0 eV) and +1.61 eV (+2.6 eV), respectively. When the AgBr/g-C_3N_4 photocatalysts were exposed to visible light, both AgBr and g-C_3N_4 could be excited to generate electron–hole pairs. According to the traditional charger carrier transfer mechanism, the photogenerated electrons in the CB of g-C_3N_4 will flow down to the CB of AgBr, and photogenerated positive carriers in the VB of AgBr will migrate to the VB of g-C_3N_4. However, considering the band structure of AgBr and g-C_3N_4, the electrons accumulated in the CB of AgBr (E_{CB} = 0.0 eV) cannot reduce O_2 to generate $\cdot O_2^-$ ($E°(O_2/\cdot O_2^-)$ = −0.33 eV), and the VB holes of g-C_3N_4 (E_{VB} = 1.61 eV) cannot oxidize OH^-/H_2O to give $\cdot OH$ (1.99 and 2.38 eV for OH^-/$\cdot OH$ and H_2O/$\cdot OH$ potential). This mechanism, therefore, is contradictory to the experimental results since both O_2^- and $\cdot OH$ are detected in our system. Instead, the experimental phenomena could be perfectly explained by a Z-scheme charge transfer mechanism (Fig. 11). The VB holes of g-C_3N_4 recombine with the photogenerated electrons in the CB of AgBr. While the electrons remain in the CB of g-C_3N_4 to reduce O_2 to yield $\cdot O_2^-$ radicals.[60,61] Meanwhile, the VB holes of AgBr oxidize OH^-/H_2O to give $\cdot OH$. Therefore, for the AgBr/g-C_3N_4 nanocomposites, the reduction active site is on the CB of g-C_3N_4 while the oxidation active site is on the VB of AgBr.

4. Conclusions

In summary, a highly efficient visible-light-driven AgBr/g-C_3N_4 hybrid photocatalyst was successfully synthesized by growth of AgBr nanoparticles on a protonated g-C_3N_4 matrix. The AgBr/g-C_3N_4 hybrid photocatalysts exhibited excellent visible-light-driven photocatalytic inactivation toward *E. coli*, which outperformed g-C_3N_4 and AgBr. The optimal AgBr loading was 30%, and 10^7 cfu mL^{-1} *E. coli* could be completely inactivated in

90 min. The remarkably enhanced photocatalytic inactivation performance was ascribed to the enhanced generation as well as suppressed recombination of photogenerated charge carriers through a Z-scheme charge transfer route. The mechanism study suggests h$^+$ was the main reactive species accounting for inactivation of *E. coli*.

Conflicts of interest

There are no conflicts to declare.

Acknowledgements

Notes and references

1 W. H. Organization and UNICEF, *Progress on Drinking Water, Sanitation and Hygiene: 2017 update and SDG baselines*, 2017.

2 Q. Li, S. Mahendra, D. Y. Lyon, L. Brunet, M. V. Liga, D. Li and P. J. J. Alvarez, *Water Res.*, 2008, **42**, 4591–4602.

3 S. Lin, R. Huang, Y. Cheng, J. Liu, B. L. T. Lau and M. R. Wiesner, *Water Res.*, 2013, **47**, 3959–3965.

4 T. Matsunaga, R. Tomoda, T. Nakajima and H. Wake, *FEMS Microbiol. Lett.*, 1985, **29**, 211–214.

5 Q. Zhou, S. Ma and S. Zhan, *Appl. Catal., B*, 2018, **224**, 27–37.

6 S. Ma, S. Zhan, Y. Jia, Q. Shi and Q. Zhou, *Appl. Catal., B*, 2016, **186**, 77–87.

7 J. Liang, F. Liu, J. Deng, M. Li and M. Tong, *Water Res.*, 2017, **123**, 632–641.

8 M. N. Chong, B. Jin, C. W. K. Chow and C. Saint, *Water Res.*, 2010, **44**, 2997–3027.

9 N. S. Lewis, *Science*, 2007, **315**, 798–801.

10 X. Bai, L. Wang, Y. Wang, W. Yao and Y. Zhu, *Appl. Catal., B*, 2014, **152–153**, 262–270.

11 H. Huang, K. Xiao, Y. He, T. Zhang, F. Dong, X. Du and Y. Zhang, *Appl. Catal., B*, 2016, **199**, 75–86.

12 H. Huang, K. Xiao, F. Dong, J. Wang, X. Du and Y. Zhang, *RSC Adv.*, 2016, **6**, 94361–94364.

13 H. Huang, X. Han, X. Li, S. Wang, P. K. Chu and Y. Zhang, *ACS Appl. Mater. Interfaces*, 2015, **7**, 482–492.

14 K. Li, Z. Zeng, L. Yan, S. Luo, X. Luo, M. Huo and Y. Guo, *Appl. Catal., B*, 2015, **165**, 428–437.

15 H. Zhao, H. Yu, X. Quan, S. Chen, Y. Zhang, H. Zhao and H. Wang, *Appl. Catal., B*, 2014, **152–153**, 46–50.

16 H. Huang, K. Xiao, N. Tian, F. Dong, T. Zhang, X. Du and Y. Zhang, *J. Mater. Chem. A*, 2017, **5**, 17452–17463.

17 K. Wang, Q. Li, B. Liu, B. Cheng, W. Ho and J. Yu, *Appl. Catal., B*, 2015, **176–177**, 44–52.

18 S. C. Yan, Z. S. Li and Z. G. Zou, *Langmuir*, 2010, **26**, 3894–3901.

19 G. Li, X. Nie, J. Chen, Q. Jiang, T. An, P. K. Wong, H. Zhang, H. Zhao and H. Yamashita, *Water Res.*, 2015, **86**, 17–24.

20 W. Wang, J. C. Yu, D. Xia, P. K. Wong and Y. Li, *Environ. Sci. Technol.*, 2013, **47**, 8724–8732.

21 Y. Li, C. Zhang, D. Shuai, S. Naraginti, D. Wang and W. Zhang, *Water Res.*, 2016, **106**, 249–258.

22 H. Li, J. Liu, W. Hou, N. Du, R. Zhang and X. Tao, *Appl. Catal., B*, 2014, **160–161**, 89–97.

23 C. Han, L. Ge, C. Chen, Y. Li, X. Xiao, Y. Zhang and L. Guo, *Appl. Catal., B*, 2014, **147**, 546–553.

24 P. He, L. Song, S. Zhang, X. Wu and Q. Wei, *Mater. Res. Bull.*, 2014, **51**, 432–437.

25 T. Zhu, Y. Song, H. Ji, Y. Xu, Y. Song, J. Xia, S. Yin, Y. Li, H. Xu, Q. Zhang and H. Li, *Chem. Eng. J.*, 2015, **271**, 96–105.

26 Y. Li, Y. Li, S. Ma, P. Wang, Q. Hou, J. Han and S. Zhan, *J. Hazard. Mater.*, 2017, **338**, 33–46.

27 Y. Song, J. Qi, J. Tian, S. Gao and F. Cui, *Chem. Eng. J.*, 2018, **341**, 547–555.

28 Y. Liu, S. Yang, S.-N. Yin, L. Feng, Y. Zang and H. Xue, *Chem. Eng. J.*, 2018, **334**, 2401–2407.

29 R. J. Deri, J. P. Spoonhower and J. F. Hamilton, *J. Appl. Phys.*, 1985, **57**, 1968–1970.

30 D. Wang, L. Guo, Y. Zhen, L. Yue, G. Xue and F. Fu, *J. Mater. Chem. A*, 2014, **2**, 11716–11727.

31 X. Wen, C. Niu, L. Zhang, C. Liang, H. Guo and G. Zeng, *J. Catal.*, 2018, **358**, 141–154.

32 J. He, Y. Cheng, T. Wang, D. Feng, L. Zheng, D. Shao, W. Wang, W. Wang, F. Lu, H. Dong, R. Zheng and H. Liu, *Appl. Surf. Sci.*, 2018, **40**, 99–106.

33 X. Wen, C. Niu, H. Guo, L. Zhang, C. Liang and G. Zeng, *J. Catal.*, 2018, **358**, 211–223.

34 X. Miao, X. Shen, J. Wu, Z. Ji, J. Wang, L. Kong, M. Liu and C. Song, *Appl. Catal., A*, 2017, **539**, 104–113.

35 T. W. Ng, L. Zhang, J. Liu, G. Huang, W. Wang and P. K. Wong, *Water Res.*, 2016, **90**, 111–118.

36 J. N. Tiwari, K. Mahesh, N. H. Le, K. C. Kemp, R. Timilsina, R. N. Tiwari and K. S. Kim, *Carbon*, 2013, **56**, 173–182.

37 Y. Feng, J. Shen, Q. Cai, H. Yang and Q. Shen, *New J. Chem.*, 2015, **39**, 1132–1138.

38 X. Miao, Z. Ji, J. Wu, X. Shen, J. Wang, L. Kong, M. Liu and C. Song, *J. Colloid Interface Sci.*, 2017, **502**, 24–32.

39 H. Katsumata, T. Sakai, T. Suzuki and S. Kaneco, *Ind. Eng. Chem. Res.*, 2014, **53**, 8018–8025.

40 W.-J. Ong, L. K. Putri, L.-L. Tan, S.-P. Chai and S.-T. Yong, *Appl. Catal., B*, 2016, **180**, 530–543.

41 C. Han, Y. Wang, Y. Lei, B. Wang, N. Wu, Q. Shi and Q. Li, *Nano Res.*, 2015, **8**, 1199–1209.

42 S. Zhou, Y. Liu, J. Li, Y. Wang, G. Jiang, Z. Zhao, D. Wang, A. Duan, J. Liu and Y. Wei, *Appl. Catal., B*, 2014, **158–159**, 20–29.

43 J. Ma, C. Wang and H. He, *Appl. Catal., B*, 2016, **184**, 28–34.

44 Z. Zhao, Y. Sun and F. Dong, *Nanoscale*, 2015, **7**, 15–37.

45 N. T. K. Thanh, N. Maclean and S. Mahiddine, *Chem. Rev.*, 2014, **114**, 7610–7630.

46 P. Niu, Y. Yang, J. C. Yu, G. Liu and H.-M. Cheng, *Chem. Commun.*, 2014, **50**, 10837–10840.

47 G. Greczynski and L. Hultman, *ChemPhysChem*, 2017, **18**, 1507–1512.

48 L. Ge, C. Han, J. Liu and Y. Li, *Appl. Catal., A*, 2011, **409–410**, 215–222.

49 Q. Xiang, J. Yu and M. Jaroniec, *J. Phys. Chem. C*, 2011, **115**, 7355–7363.

50 Y. Cui, J. Zhang, G. Zhang, J. Huang, P. Liu, M. Antonietti and X. Wang, *J. Mater. Chem.*, 2011, **21**, 13032–13039.

51 Y. Yang, Y. Guo, F. Liu, X. Yuan, Y. Guo, S. Zhang, W. Guo and M. Huo, *Appl. Catal., B*, 2013, **142–143**, 828–837.

52 B. Z. Ristic, M. M. Milenkovic, I. R. Dakic, B. M. Todorovic-Markovic, M. S. Milosavljevic, M. D. Budimir, V. G. Paunovic, M. D. Dramicanin, Z. M. Markovic and V. S. Trajkovic, *Biomaterials*, 2014, **35**, 4428–4435.

53 Z. Liu, W. Guo, C. Guo and S. Liu, *RSC Adv.*, 2015, **5**, 72872–72880.

54 C. Tang, H. Bai, L. Liu, X. Zan, P. Gao, D. D. Sun and W. Yan, *Appl. Catal., B*, 2016, **196**, 57–67.

55 S. Yang, W. Zhou, C. Ge, X. Liu, Y. Fang and Z. Li, *RSC Adv.*, 2013, **3**, 5631–5638.

56 S. Krishna, S. Maslov and K. Sneppen, *PLoS Comput. Biol.*, 2007, **3**, e41.

57 A. Muela, J. M. García-Bringas, I. Arana and I. Barcina, *Microb. Ecol.*, 2000, **40**, 336–344.

58 Y. Chen, B. Wang, S. Lin, Y. Zhang and X. Wang, *J. Phys. Chem. C*, 2014, **118**, 29981–29989.

59 C. Ye, J.-X. Li, Z.-J. Li, X.-B. Li, X.-B. Fan, L.-P. Zhang, B. Chen, C.-H. Tung and L.-Z. Wu, *ACS Catal.*, 2015, **5**, 6973–6979.

60 S. Yin, J. Han, T. Zhou and R. Xu, *Catal. Sci. Technol.*, 2015, **5**, 5048–5061.

61 H. Huang, X. Li, J. Wang, F. Dong, P. K. Chu, T. Zhang and Y. Zhang, *ACS Catal.*, 2015, **5**, 4094–4103.

62 H. Huang, S. Tu, C. Zeng, T. Zhang, A. H. Reshak and Y. Zhang, *Angew. Chem., Int. Ed.*, 2017, **56**, 11860–11864.

63 H. Huang, Y. He, X. Li, M. Li, C. Zeng, F. Dong, X. Du, T. Zhang and Y. Zhang, *J. Mater. Chem. A*, 2015, **3**, 24547–24556.

64 H. Huang, A. H. Reshak, S. Auluck, S. Jin, N. Tian, Y. Guo and Y. Zhang, *J. Phys. Chem. C*, 2018, **122**, 2661–2672.